Indonesian Journal of Science & Technology

Journal homepage: http://ejournal.upi.edu/index.php/ijost/

Computational Analysis of Different Turbulence Models in a Vane Pump Simulation

Daniel Alberto Beleño Molina[1], Rafael Ramírez Restrepo[1], Jorge Eliecer Duarte Forero[1], Andrés David Rodríguez Toscano[2]*

[1]Departamento de Ingeniería Mecánica, Universidad del Atlántico, Colombia

[2] Departamento de Energía, Universidad de la Costa, Colombia

Correspondence E-mail: arodrigu83@cuc.edu.co

ABSTRACTS

The study presents a computational analysis of a vane pump using two different turbulence models namely κ-ε and κ-ω. The geometry characteristics of the vane pump were obtained by disassembly and further measurements. The CAD model for the computational domain was developed in SOLIDWORKS®. The CFD modeling was powered by ANSYS®, which allowed the evaluation of different mesh types and turbulence models. A total set of six simulations were performed to obtain comparison schemes for turbulence model evaluation. Specifically, the angular velocity and excentricity were varied within the simulations. Both turbulence models were carefully validated using the manufacturer´s dataset as validation criteria, obtaining a relative error of less than 5%. The κ-ω experienced the best performance when describing the flow variables, excepting the pressure gradient. Specifically, the κ-ω presented an accurate prediction of edge effects, energy losses in the walls, and turbulent viscosity. Notably, the CFD modeling showed that density and velocity variations are not significant. Overall, CFD modeling demonstrated to be a robust tool to gain insight understanding of the flow interactions in vane pump operation.

ARTICLE INFO

Article History:
Received 07 Aug 2020
Revised 28 Jan 2021
Accepted 31 Jan 2021
Available online 04 Feb 2021

Keywords:
CAD modeling,
CFD modeling,
Hydroxyapatite,
Eccentricity,
Turbulence model,
Vane pump.

1. INTRODUCTION

Vane pumps can be classified on the rotary pump group and they are widely implemented in oil-hydraulic systems operating with low viscosity fluids. The massive utilization of vane pumps is supported by the wide operating range and low maintenance cost. Moreover, the mechanical efficiency of vane pumps is around 20% higher than gear pumps. Therefore, this type of equipment presents an improved techno-economic performance compared to other pumps.

Particularly, the mechanical performance evaluation of vane pumps has been developed by relating vane pump elements (loading and unloading couplings), elliptical cavity eccentricity, and vane width. On the other hand, it is important to relate the flow interactions inside the vane pump which defines to a great extent the hydraulic performance. From an analytical approach, it is possible to model the turbulence interactions inside the pump using mathematical or statistical models that solve the Navier-Stokes equations; however, the solution by conventional methods is complex and, in some cases, not accurate. An alternative solution is the use of computational tools for simulation-based on turbulence models that considerably simplify the problem with accurate predictions. Therefore, CFD tools stand as a suitable mechanism to enhance the design evaluation and further propose system improvements (Ahmed & Demoulin, 2002). Specifically, a direct numerical solution of the Navier-Stokes equations would involve the application of hundreds of millions of finite elements to observe a detailed behavior of the different swirl scales, which limits the overall performance of the pump. Hence, additional ways of solving this problem have been developed, which provide averages and approximations of the general behavior of larger finite volumes, adding other equations that close the system and thus complete the number of equations relate to the number of unknowns.

Turbulence models must be considered in detail for the simulation in vane pumps. However, some studies do not characterize the mesh generation while the solution algorithm is not considered thoroughly. Several turbulence models are displayed in the literature and the appropriate selection is a determinant factor for a successful simulation. Such simulation must ensure that the results are consistent for the real performance of the flow systems, especially when dealing with high pressure-mass flow ratios which foster the creation or destruction of swirls in different speeds and quantities (Feng *et al.*, 2010; Lan *et al.*, 1997; Mangani *et al.*, 2011). Overall, there is a wide variety of turbulence models, but yet there are no clear criteria to define which one displays the best performance when modeling the flow interactions of vane pumps (Feng *et al.*, 2010; Lan *et al.*, 1997; Mangani *et al.*, 2011).

In the specific case of displacement pumps, Frosina *et al.* (2014) carried out a CFD modeling to simulate a double stage gear pump; in their study, they noted that by using free software, they found results very close to the real behavior of the pump, which serves as a valid tool for the design and improvement of the pump. On the other hand, some studied the fluid cavitation in a vane pump using multiple software. The study generated a dynamic deformation of the mesh in the presence of rounding at the tip of the vane. The results stated that the curvature is inversely related to the size of the cavitating region. Moreover, used different turbulence models for different nodal field regions, allowing reliable reproduction of the cavitation phenomenon in a gear pump. Simulated under the standard model κ-ε the flow inside a

DOI: http://dx.doi.org/10.17509/ijost.v6i1.xxxx |
p- ISSN 2528-1410 e- ISSN 2527-8045 |

centrifugal pump using FLUENT® software. The results displayed predominant accuracy when compared with experimental data. On the other hand, Chima (1995) proposed a κ-ω turbulence model to solve the Navier-Stokes equations for turbo-machinery elements such as compressors and turbines.

The aforementioned investigations implemented different CFD software tools. Based on the software used, the structure of the algorithm of the solution will be given, which should preferably be as simple as possible for the user. Frosina *et al.* (2014) implemented PumpLinx® to develop the CAD design of the pump and Simerics® to create the computational domain for CFD modeling. In contrast, developed the CAD design using SOLIDWORKS® to simulate the Newtonian fluid flow behavior in external gear pumps type positive displacement pump. A computer model was developed using ANSYS® software for spur gearboxes lubrication, simulating the behavior of the elastohydrodynamic lubrication film in terms of pressure and film thickness.

The aim of this research work lies in the incorporation of comparison schemes to evaluate the performance of different turbulence models while describing the hydraulic performance of a vane pump. The variation of system parameters such as angular speed and eccentricity stand as a differential factor in the CFD evaluation of vane pumps. Therefore, this work contributes to close the knowledge gap regarding turbulence model evaluation when analyzing the overall performance of a vane pump. A complete characterization of the CAD design and CFD formulation is incorporated in the analysis.

2. METHODS AND MATERIALS

The turbulence models described in the specialized literature, the dimensional modeling of the selected vane pump in SOLIDWORKS®, and the methodology used for the elaboration of the CFD model with ANSYS® are shown in this section.

2.1. Turbulence models

To solve the turbulence interactions in a fluid, a set of equations must be established to completely solve all the properties of the system, more specifically its kinematics and dynamics characteristics. Thus, Reynolds Transport Theorem is used, which is a mechanism that converts a general analysis of a system to a control volume analysis, with variations related to whether the control volume is fixed, deformable, or in motion. The interest will be focused on the case of deformable control volume and with arbitrary motion since it will be the basis of the Naiver Stokes equations. The starting point is the equation provided by Reynolds' transport theorem regarding volume and mass flow rate. This formulation establishes a cubic differential element and solves it under the principle of conservation of mass. It is possible to obtain the continuity equation [1], written in the clearest way as:

$$\frac{\partial \rho}{\partial t} + \nabla \cdot (\rho V) = 0 \qquad (1)$$

By applying the concept of moment flow to a cubic differential element, all types of forces involved in that system must be assumed, being the body forces and the surface forces. Considering that the only external field is the gravitational one, whereas surface forces are due to stresses on all sides of the control surface, i.e., the sum of hydrostatic pressure and viscous stresses. It is possible to obtain the linear momentum equation [2, 3] in the simplest form as:

$$\rho g - \nabla p + \nabla \cdot \tau_{ij} = \rho \frac{dV}{dt} \qquad (2)$$

where:

$$\frac{dV}{dt} = \frac{\partial V}{\partial t} + u\frac{\partial V}{\partial x} + v\frac{\partial V}{\partial y} + w\frac{\partial V}{\partial z} \qquad (3)$$

Considering that, for a Newtonian fluid, the viscous stresses are proportional to the strain rate and the viscosity coefficient, it is

possible to achieve results that rewrite the momentum equation developed, which by substituting in the moment equation generate the Navier-Stokes equations [4, 5 & 6], written in the easiest way as:

$$\rho g_x - \frac{\partial p}{\partial x} + \mu\left(\frac{\partial^2 u}{\partial x^2} + \frac{\partial^2 u}{\partial y^2} + \frac{\partial^2 u}{\partial z^2}\right) = \rho\frac{du}{dt} \quad (4)$$

$$\rho g_y - \frac{\partial p}{\partial y} + \mu\left(\frac{\partial^2 v}{\partial x^2} + \frac{\partial^2 v}{\partial y^2} + \frac{\partial^2 v}{\partial z^2}\right) = \rho\frac{dv}{dt} \quad (5)$$

$$\rho g_z - \frac{\partial p}{\partial z} + \mu\left(\frac{\partial^2 w}{\partial x^2} + \frac{\partial^2 w}{\partial y^2} + \frac{\partial^2 w}{\partial z^2}\right) = \rho\frac{dw}{dt} \quad (6)$$

Depending on the complexity of the differential equations found to solve the problem of fluid turbulence in an analytical way, throughout history, many researchers have set themselves the task of establishing turbulence models, which somehow simplify the phenomenon and solve the situation in a compact way. Usually, the turbulence is computationally solved, establishing models that differ in the number of differential equations intended to be solved. In this sense, there are models with a single differential equation and more robust models of up to 7 differential equations to be solved. For strictly academic purposes, the researcher's purpose was to establish an overview of the problem of turbulence. Therefore, the turbulence model κ-ε and the turbulence model κ-ω were chosen, where κ is turbulent kinetic energy, ε is the dissipation of turbulent kinetic energy and ω is the frequency of turbulent kinetic energy. The model of Launder-Sharma (1974), known as the standard κ-ε model is presented below:

Kinematic viscosity of swirl equation [7]:

$$\upsilon_T = C_\mu \frac{\kappa^2}{\epsilon} \quad (7)$$

Turbulent kinetic energy equation [8]:

$$\frac{\partial \kappa}{\partial t} + U_j \frac{\partial \kappa}{\partial x_j} = \tau_{ij}\frac{\partial U_i}{\partial x_j} - \epsilon + \frac{\partial}{\partial x_j}\left[\left(\upsilon + \frac{\upsilon_T}{\sigma_k}\right)\frac{\partial \kappa}{\partial x_j}\right] \quad (8)$$

Dissipation rate equation [9]:

$$\frac{\partial \epsilon}{\partial t} + U_j \frac{\partial \epsilon}{\partial x_j} = C_{\epsilon 1}\frac{\epsilon}{k}\tau_{ij}\frac{\partial U_i}{\partial x_j} - C_{\epsilon 2}\frac{\epsilon^2}{k} + \frac{\partial}{\partial x_j}\left[\left(\upsilon + \frac{\upsilon_T}{\sigma_\epsilon}\right)\frac{\partial \epsilon}{\partial x_j}\right] \quad (9)$$

Closing coefficient and auxiliary ratios equation [10]:

$$C_{\epsilon 1} = 1.44, \quad C_{\epsilon 2} = 1.92, \quad C_\mu = 0.09, \quad \sigma_k = 1.0$$
$$\sigma_\epsilon = 1.3, \ \omega = \frac{\epsilon}{C_\mu \kappa}, \ l = C_\mu \frac{\kappa^{3/2}}{\epsilon} \quad [10]$$

The following is Wilcox's model, known as the κ-ω model:

Kinematic viscosity of swirls equation [11, 12]:

$$\upsilon_T = \frac{\kappa}{\tilde{\omega}} \quad (11)$$

where:

$$\tilde{\omega} = max\left\{\omega, \ C_{lim}\sqrt{\frac{2S_{ij}S_{ij}}{\beta^*}}\right\}, \quad C_{lim} = \frac{7}{8} \quad (12)$$

Turbulent kinetic energy equation [13]:

$$\frac{\partial \kappa}{\partial t} + U_j \frac{\partial \kappa}{\partial x_j} = \tau_{ij}\frac{\partial U_i}{\partial x_j} - \beta^*\kappa\omega + \frac{\partial}{\partial x_j}\left[\left(\upsilon + \sigma^*\frac{\kappa}{\omega}\right)\frac{\partial \kappa}{\partial x_j}\right] \quad (13)$$

DOI: http://dx.doi.org/10.17509/ijost.v6i1.xxxx |
p- ISSN 2528-1410 e- ISSN 2527-8045 |

Specific dissipation rate equation [14]:

$$\frac{\partial \omega}{\partial t} + U_j \frac{\partial \omega}{\partial x_j} = \alpha \frac{\omega}{\kappa} \tau_{ij} \frac{\partial U_i}{\partial x_j} - \beta \omega^2 + \frac{\sigma_d}{\omega} \frac{\partial \kappa}{\partial x_j} \frac{\partial \omega}{\partial x_j} + \frac{\partial}{\partial x_j} \left[\left(\upsilon + \sigma \frac{\kappa}{\omega} \right) \frac{\partial \omega}{\partial x_j} \right] \quad (14)$$

Closing coefficient and auxiliary ratios equation [15]:

$$\alpha = \frac{13}{25}, \qquad \beta = \beta_o f_\beta, \qquad \beta^* = \frac{9}{100},$$

$$\sigma = \frac{1}{2}, \qquad \sigma^* = \frac{3}{5}, \qquad \sigma_{do} = \frac{1}{8}$$

$$\sigma_d = \begin{cases} 0, & \frac{\partial \kappa}{\partial x_j} \frac{\partial \omega}{\partial x_j} \leq 0 \\ \sigma_{do}, & \frac{\partial \kappa}{\partial x_j} \frac{\partial \omega}{\partial x_j} > 0 \end{cases}$$

$$\beta_o = 0.0708, \qquad \epsilon = \beta^* \omega \kappa, \qquad l = \frac{\kappa^{1/2}}{\omega}$$

$$f_\beta = \frac{1+85\chi_\omega}{1+100\chi_\omega}, \ \chi_\omega \equiv \left| \frac{\Omega_{ij}\Omega_{jk}S_{ki}}{(\beta^*\omega)^3} \right| \quad (15)$$

The tensors Ω_{ij} and S_{ki} are the mean rotation tensor and the mean strain rate tensor, respectively, defined as equation [16]:

$$\Omega_{ij} = \frac{1}{2}\left(\frac{\partial U_i}{\partial x_j} - \frac{\partial U_j}{\partial x_i} \right), S_{ki} = \frac{1}{2}\left(\frac{\partial U_i}{\partial x_j} + \frac{\partial U_j}{\partial x_i} \right) \quad (16)$$

2.2. Vane pump modeling

In order to develop the CFD modeling, quantitative research was proposed because a logical and ordered sequence of steps is required to achieve the proposed general objective. The cycle proposed by Bathe was implemented who proposes a feedback relationship between the computer model and the simulation. The steps that were necessary to carry out the investigation are shown below.

2.2.1. Disassembly stage.

According to the available information about vane pumps on the market, accessibility and reports in the specialized literature (Inaguma, 2010), a pre-commanded variable flow unbalanced vane pump, model PV7-1A/40-45RE37MD0-16 from the manufacturer Rexroth® was selected.

Figure 1 shows the complete disassembly of the pump used in the study; a full disassembly of all the parts was accomplished so that measurements could be taken to develop the CAD design using SOLIDWORKS®. Based on the information provided in the official catalog (Dimensions) and the measurements collected with the gauges and dial indicators, the measurements taken were systematically documented.

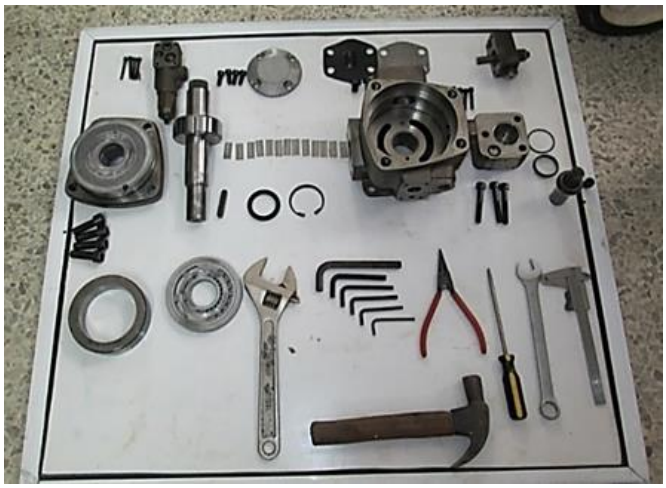

Figure 1. Complete disassembly of the pump.

2.2.2. CAD development process

The schematics of the vane pump model developed in SOLIDWORKS® is shown in **Figure 2**. It should be acknowledged that, in the final assembly of all the parts, many position relations were necessary, which were: 21 of the concentric type, 2 of the tangent type, 49 of the coincident type, 6 of the parallel type, 40 of the tangent cam-type, 1 of the concentric cam type and 23 of the width type.

One of the biggest challenges in the CAD design of the pump was to ensure that each vane made constant contact with the stator once the rotor was rotating. Thus, a modification of the vane geometry was taken into account consisting of a very small triangular end just at the edge of the vane so that only one line makes contact with the stator. **Figure 2 (right)** provides a slice view to illustrate the eccentric volume chamber, and the latter modification; note that the side of the vane is actually rectangular, and the stator, due to its eccentric nature, has a curved surface, so there is no way to fit a position relation that takes this condition into the program used.

The control volume inside the chamber is based on the space between the vanes, the stator, the rotor, and the main housing. A control volume for the entire input and output streams should also be considered. Due to the complexity of the geometry used, it is necessary to use the complement *Flow simulation* to use the tool, *lid,* which is able to generate boundary layers over the CAD once unnecessary parts are removed for the study.

Figure 3 shows the fluid control volume, which is imported directly into the ANSYS® for the respective CFD modeling. In **Figure 4,** two-volume chambers with different types of eccentricity are presented since the aim is to analyze the variation of pump eccentricity. According to the CAD geometry, the measurement range where the position of the stator is likely to fluctuate is almost 2 mm, because when the stator is concentric with the housing, the measurements indicate that it can only be moved 2 mm to the right or left.

According to **Figure 4,** the volume profile generated in the eccentric chamber is shown in the foreground, and some of the fluid trapped between the main cover and the vanes is shown behind. This space is actually very small compared to the space produced between the vane, rotor, and stator, but it is still part of the fluid control volume.

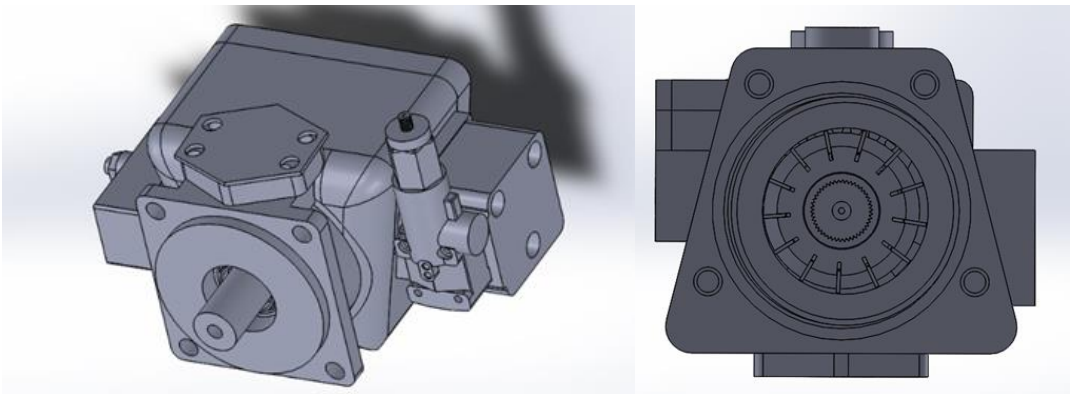

Figure 2. Left: CAD overview of the pump used, right: CAD eccentric volume chamber.

DOI: http://dx.doi.org/10.17509/ijost.v6i1.xxxx |
p- ISSN 2528-1410 e- ISSN 2527-8045 |

2.2.3. CFD modeling

Once the generated CAD has been imported, it is modified in the design modeler tool in order to proceed with the definition of the specific parts of the solid with assigned names, in other words, to formally define the input and output in the pump. **Figure 5** shows the cut-off view of the total meshing control volume for the execution of a fine mesh.

Then, according to the FLUENT tool, there are 63421 nodes, distributed in tetrahedral cells, IDS partition cells, mixed wall sides, triangular inner sides, wall sides, interface sides, input and output sides, side and metric data interfaces; all of the above must be modified to establish the correct model, material and border conditions.

Regarding the working fluid, a mineral oil HLP, according to DIN 51524, is required. Shell Tellus S2 V 68 (previously Shell Tellus T), manufactured by Shell Lubricants, is chosen. It is regulated by ISO 4406 class 21/19/16, which is the equivalent in Colombia to DIN 51524.

According to the official catalog, the operating density (for 15°C) is 877 kg/m^{3,} and the kinematic operating viscosity (for 50°C) is $4.1x10^{-5}$ m^2/s. Using the dynamic viscosity ratio gives μ = ρv = 0,035957 kg/m·s. Note that a different value was used to calculate the density kinematic viscosity, because theoretically, the same properties should be used at the same temperature, but actually the expansion coefficient for mineral oils is around $7x10^{-4}\ K^{-1}$, which means that the volume expands only 0.7% when the temperature increases by 10°C; this means that practically the density remains constant in a high range of operating temperature, but the viscosity changes radically for small ranges of temperature, for that reason, the manufacturer's rheology graph was used. Concerning the boundary conditions, the information was taken from the official catalogs (Rexroth, 2012) in general, with SOLIDWORKS® it is possible to measure the input area, resulting in $7.0497x10^{-4}\ m^2$.

For the first and second models at the output, there is a maximum operating pressure of 160 bar. Similarly, for the input, the pump has to handle a flow rate of $66\ L/min = 0.0011\ m^3/s$, measured with an angular speed of 1450 rpm, the pressure of 10 bar and viscosity of $41\ mm^2/s$ (at 50°C). So, as the density does not change, the fluid inlet speed for these conditions is 1.56035 m/s, and a mass flow of 0.9647 kg/s. For the third and fourth models, the outlet has a maximum operating pressure of 140 bar. For the inlet, the pump has to handle a flow rate of $79.6\ L/min = 0.0013267\ m^3/s$, measured with an angular speed of 1750 rpm, the pressure of 10 bar and viscosity of $41\ mm^2/s$ (at 50°C). Similarly, the inlet velocity is 1.8818767 m/s, and mass flow is 1.163487 kg/s.

For the fifth and sixth model, when varying the eccentricity, the following expression can be used equation [16]:

$$Q = \frac{2 \cdot e \cdot b \cdot \pi (d-e) \cdot n}{60} \qquad (16)$$

where: e is the eccentricity, b is the rotor width, d is the stator diameter, and n is the angular velocity. According to SOLIDWORKS®, b = 31.17 mm, d = 121.055 mm. Immediately it is verified that when entering the eccentricity of 2 mm (maximum) exactly the same flow rate is obtained as that offered by the pump, showing the validity of the equation. Therefore, by modifying for an eccentricity of 1 mm, a flow rate of 0.000568216 m^3/s is obtained, which is the same as approximately 34.1 l/min; consequently, an input speed of 0.806015 m/s with a mass flow of 0.498326 kg/s keeping the same input area of $7.0497x10^{-4}\ m^2$. To sum up, **Figure 7** shows an illustration referring to the final form of the study schematic, where the tools mentioned above are clearly shown in a sequential and practical way; there are two work schemes for each type of model carried

out as required, note the blue links within the boxes of each operation, which refer to the operation carried out directly to the other work environment, in order to not repeat the operation.

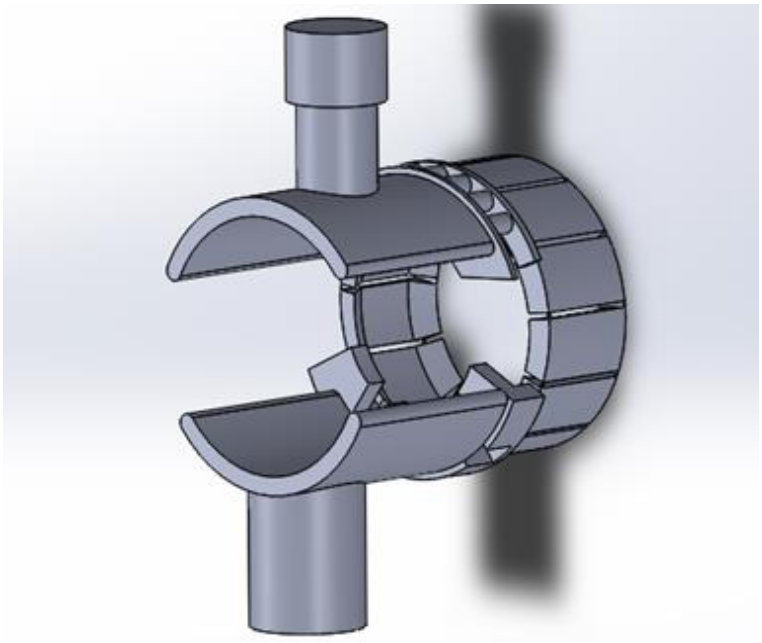

Figure 3. Fluid control volume.

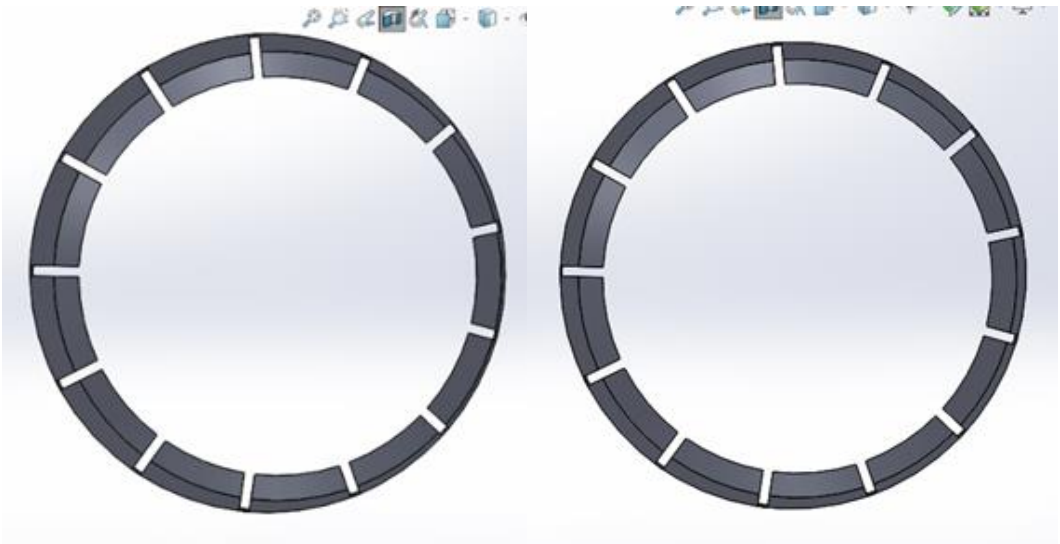

Figure 4. Sectional view of the respective chamber volumes for 2 mm eccentricity (top) and 1 mm eccentricity (bottom).

DOI: http://dx.doi.org/10.17509/ijost.v6i1.xxxx |
p- ISSN 2528-1410 e- ISSN 2527-8045 |

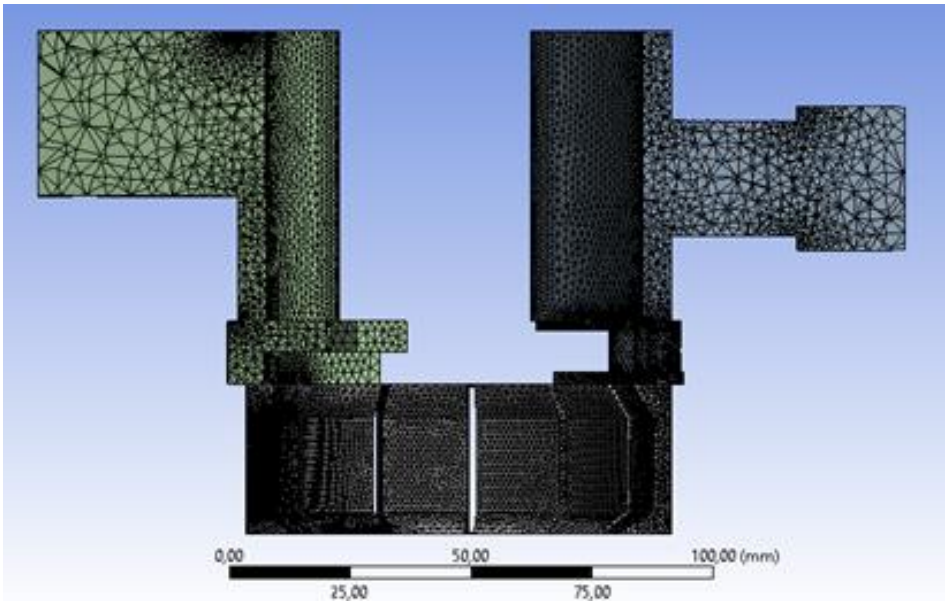

Figure 5. Sectioned view of the control volume mesh.

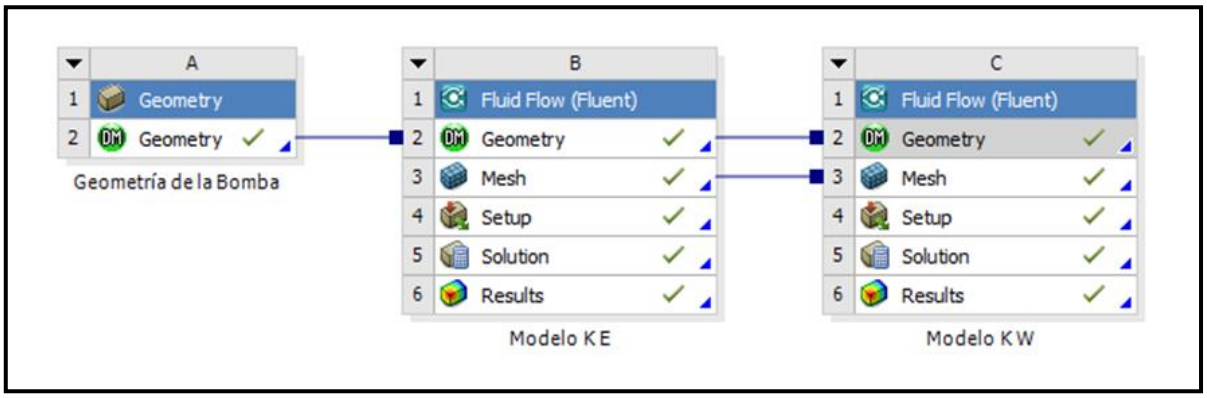

Figure 7. Schematic of the overall study.

3. RESULTS AND DISCUSSION

In this section, the selected turbulence models are evaluated. The boundary conditions are set by the pump's manufacturer. For this purpose, the model κ-ε and κ-ω were evaluated to verify how close response is reached, in order to give a validation criterion for the simulation performed. Moreover, two additional simulations are included for the two models in which the angular rotation speed is modified. Finally, another two case studies are incorporated by modifying the eccentricity.

3.1. Conventional κ-ε model simulation

The main parameter examined for the model validation is the pressure range within the pump. The output pressure profile is displayed in **Figure 8 (left)**. Although the output profile shows a variation in colors, the contour indicator reveals a compact value for the pressure since it is the same at all points. From this profile, it is noticeable that the output pressure is approximate $1.63431x10^7$ Pa, which is more about 163 bar. Considering the operating output pressure, under the same conditions, it offers a value of 160 bar. Therefore, the relative percentage error is:

$$E\% = \frac{|163\ bar - 160\ bar|}{160\ bar} * 100\% = 1.875\%$$

A relative error of 1.875% corroborates the consistency of the calculations. Therefore, the simulation is satisfactorily validated under this parameter. According to **Figure 8 (right)**, the speed profile reports some kind of concentric symmetry, although some disordered can be observed on the right side with an increasing magnitude trend in the center.

Density calculations are shown in **Figure 9**, where it can be seen that it does not change at all under the conditions set out in the simulation. The pressure profile in the main chamber is shown in **Figure 10 (left)**.

Figure 10 (left) shows the profile for the internal chamber pressure of the first model. This reveals two important zones: a blue one (suction zone, because it has vacuum pressure) and an orange one (discharge zone, high pressure), revealing what happens in practice concerning this physical phenomenon.

Notice the variation in viscosity in the same chamber **(right Figure 10)**. Note that turbulent viscosity in the suction area is where the highest values occur and the lower values in the discharge area because the fluid must move more easily in the discharge than in the suction. The results obtained for the sectional view of the inlet, outlet, and internal chamber, relating to pressure, turbulent kinetic energy, and dissipation of turbulent energy is shown in **Figure 11**.

Figure 11 indicates that, for the established conditions, the pressure has high values at the outlet and lower values at the inlet within the three views. The latter reaffirms what is expected in the simulation; furthermore, in the central image, the profile related to the shape of the pump's rotation can be seen, as the pressure transition can be seen on the suction and discharge channel. For the profiles of turbulent kinetic energy and dissipation of turbulent energy, it is highlighted that they all have in common, for its central and left image, an increase in each property in the suction zone, revealing once again the critical state of the fluid when it undergoes this phase; in a similar way, according to the images on the right for all the properties, it can be seen that the variations are mainly shown in the changes of geometry since basically the border effects in the turbulence are what generate these abrupt changes.

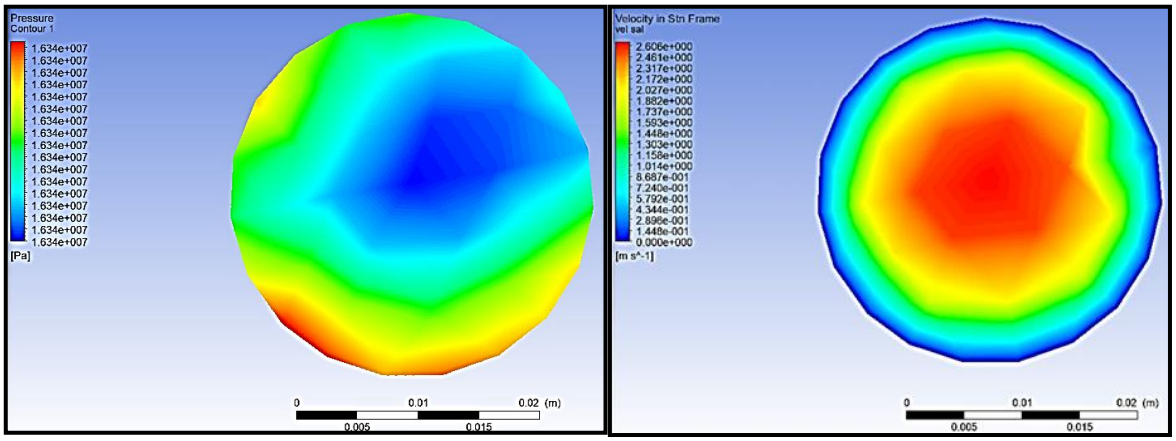

Figure 8. First model – left: Outlet pressure profile, right: Outlet speed profile.

DOI: http://dx.doi.org/10.17509/ijost.v6i1.xxxx |
p- ISSN 2528-1410 e- ISSN 2527-8045 |

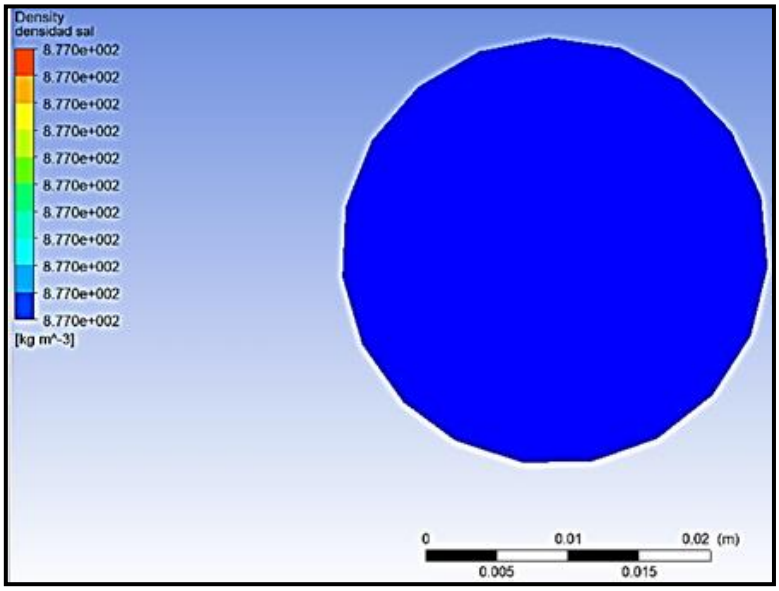

Figure 9. Density profile at the output, first model

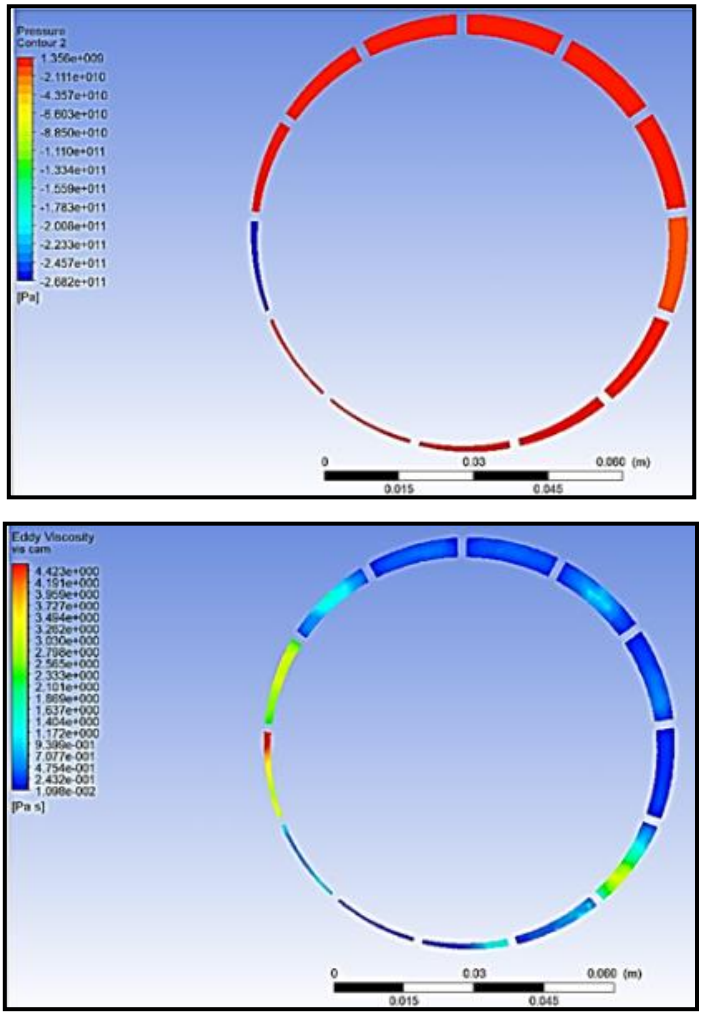

Figure 10. First model - Left: Pressure profile for the internal chamber, Right: Turbulent viscosity profile, for the inner chamber.

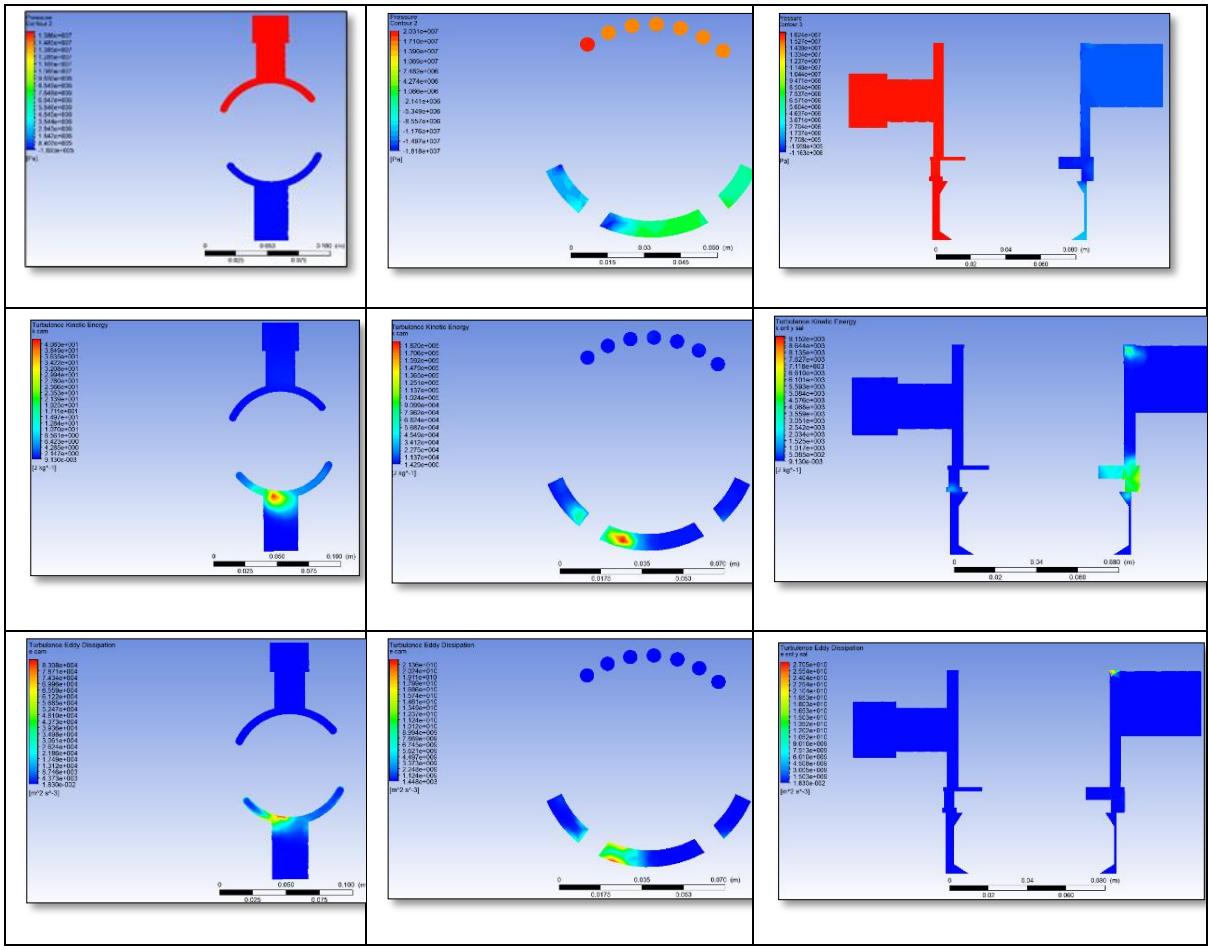

Figure 11. Pressure profiles, turbulent kinetic energy and dissipation of turbulent energy, in consecutive order respectively, sectional view of chamber, inlet and outlet, first model.

3.2. κ-ω model simulation

Similarly, the output pressure is verified, resulting in the profile in **Figure 12 (left)**. From this profile, it can be seen that the output pressure is approximate $1.66836x10^7$ Pa, which is approximately 167 bar. Considering the operating output pressure, under the same conditions, it gives a value of 160 bar which results in the following relative error:

$$E\% = \frac{|167\ bar - 160\ bar|}{160\ bar} * 100\% = 4.375\%$$

A relative percentage error of 4.375% was found, which is considerably higher compared to the k-ε model. Since the error is less than 5%, the simulation is successfully validated under this parameter. Afterward, the speed profile can be seen in **Figure 12 (right)**. Accordingly, the values are very close between the two models, keeping a more random but concentric profile at the output.

From now on, density-related results are omitted for all simulations since this value did not change. The pressure profile for the internal chamber is displayed in **Figure 13 (left)**. Definitely, the profile for the pressure was not the most realistic to the phenomenon that occurs because it does not clearly define the areas of suction and discharge in the pressure gradients. For convenience purposes, the results of this and other simulations referring to density will be omitted, since under everything previously mentioned, the variables of dissipation of turbulent energy, ε, (for the model κ-ε) and the frequency of turbulent energy, ω, (for the model κ-ω) will not be changed, as both

DOI: http://dx.doi.org/10.17509/ijost.v6i1.xxxx |
p- ISSN 2528-1410 e- ISSN 2527-8045 |

magnitudes basically refer to the same concept, related to the temporal distribution of the turbulent kinetic energy, so it is enough to appreciate the colored contour for the turbulent kinetic energy, κ, in each model. For turbulent viscosity **(Figure 13 at right)**, a higher value in the suction area is maintained, and in fact, a better profile is formed that shows this transition but does not show results for the discharge area.

Similarly, **Figure 14** shows a sectional view of the inlet, outlet, and internal chamber in terms of pressure and turbulent kinetic energy.

Figure 14 shows similar results to those obtained with the first model for the pressure gradient, as in the three views, the high and low pressures are differentiated, and in the central image, the transition of pressures in the suction and discharge line can be seen, and in fact, it is better defined with respect to the previous model, even for the image on the right, because it clearly defines what happens at the entrance and exit of the rotating volume. Additionally, the turbulent kinetic energy shows the same resemblance as before, in all the images, there is an increase in each property in the suction area, and the profiles in each property are much better defined with respect to the previous model since details are defined in the section changes of the geometry having results closer to what would be the real profile of the situation.

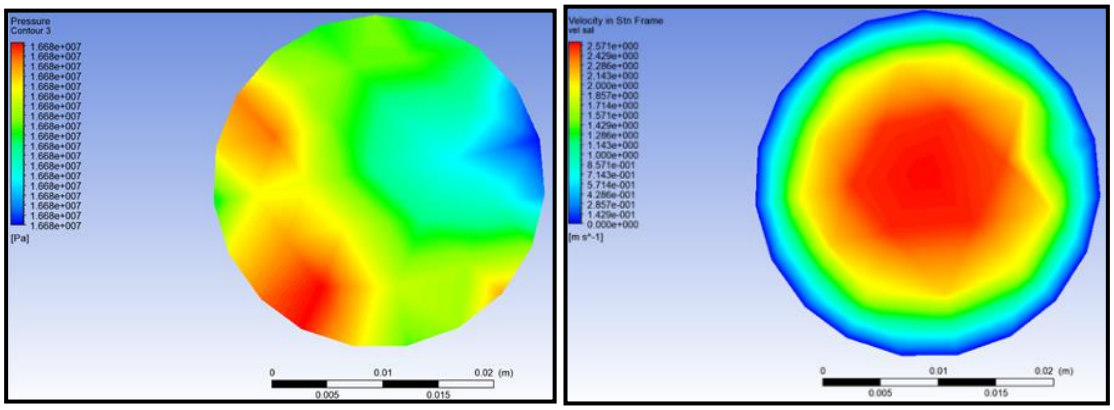

Figure 12. Second model – left: Outlet pressure profile, right: Speed profile at the output.

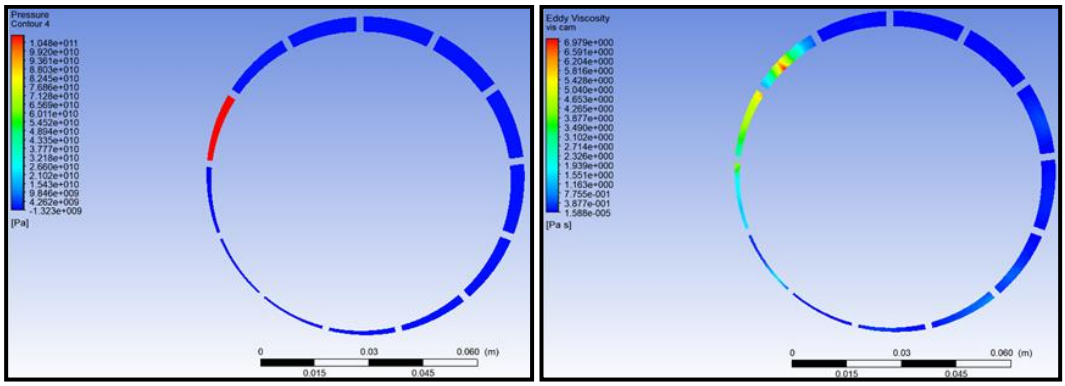

Figure 13. Left: Pressure profile for the internal chamber, first model, right: Turbulent viscosity profile, for the inner chamber, first model.

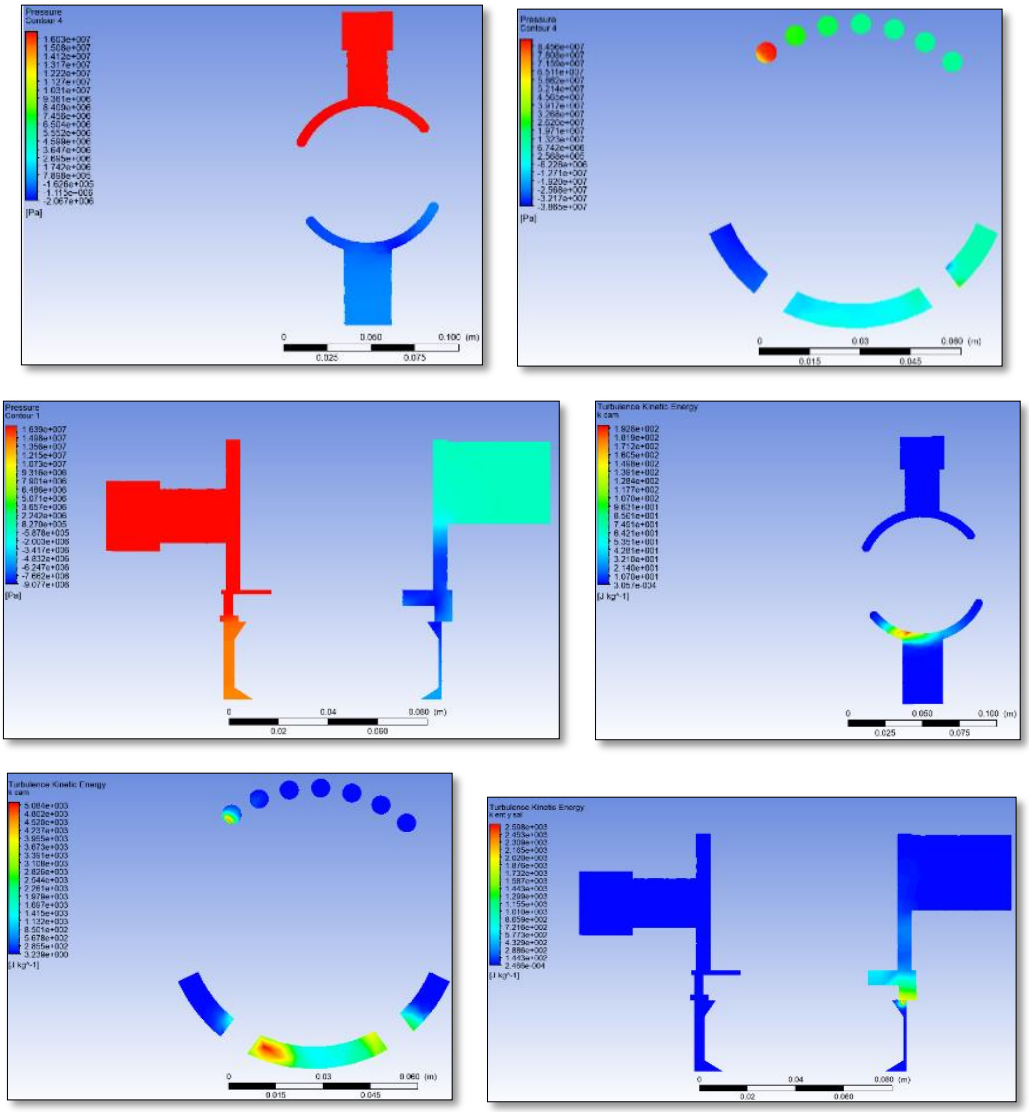

Figure 14. Pressure profiles, turbulent kinetic energy and dissipation of turbulent energy, in consecutive order respectively, sectional view of chamber, inlet and outlet, first model.

3.3. Third model, carried out with κ-ε

As in the previous two cases, the aim is to validate the simulation, so the outlet pressure profile is presented in **Figure 15 (left)**. For the following two models, a modification was carried out to the shape of the boundary conditions without changing their value, and this generated quite remarkable changes in the profiles found. Note that for the output profile, there is a different distribution compared to the previous simulations because there are areas with lower pressures, accompanied by high pressures, on average, an output pressure of approximately $1.424544x10^7$ Pa was obtained, which is more approximately 142 bar:

Considering the operating output pressure, under the same conditions, it offers a value of 140 bar. Therefore, the relative percentage error is:

$$E\% = \frac{|142\ bar - 140\ bar|}{140\ bar} * 100\% = 1.428\%$$

DOI: http://dx.doi.org/10.17509/ijost.v6i1.xxxx |
p- ISSN 2528-1410 e- ISSN 2527-8045 |

A relative percentage error of 1.428% was found, less than 5%. Therefore, the simulation is satisfactorily validated under this parameter.

A more suitable result for the simulation is presented, as it has a profile with greater kinematic variations, conserving the concentric characteristic. According to **Figure 16 (left)**, the pressure is defined a little better in the suction port and the intake port in the chamber, but it still has some weaknesses related to the total definition of the profile. Concerning the turbulent viscosity, **Figure 16 (right)** shows high magnitude values near the most eccentric areas of the chamber, making them more resistant to flow. Next, there is a sectional view of the inlet, outlet, and internal chamber, referring to pressure and turbulent kinetic energy, as shown in **Figure 17**. The difference is clear for this case; for the pressure in this model, the profile at the output is clearly defined, showing the appropriate range of interest for the response in this simulation, and below the central image, the high and low pressure is shown correctly.

Finally, for the turbulent kinetic energy, clear energy zones can be seen at the suction points because these points are the ones that lose the most energy due to the chaotic state of the fluid at these points, as a result of sudden changes in the section area.

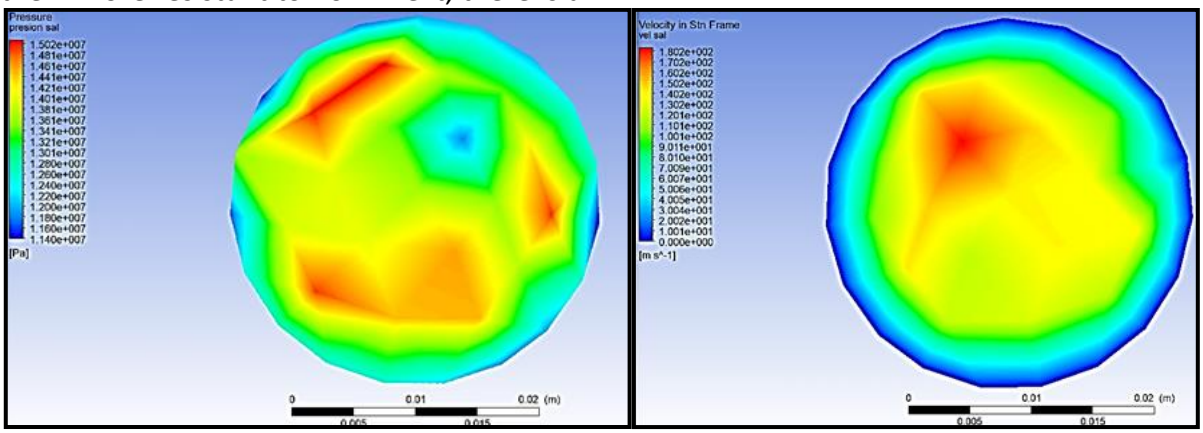

Figure 15. Third model – left: Outlet pressure profile, right: Speed profile at the output.

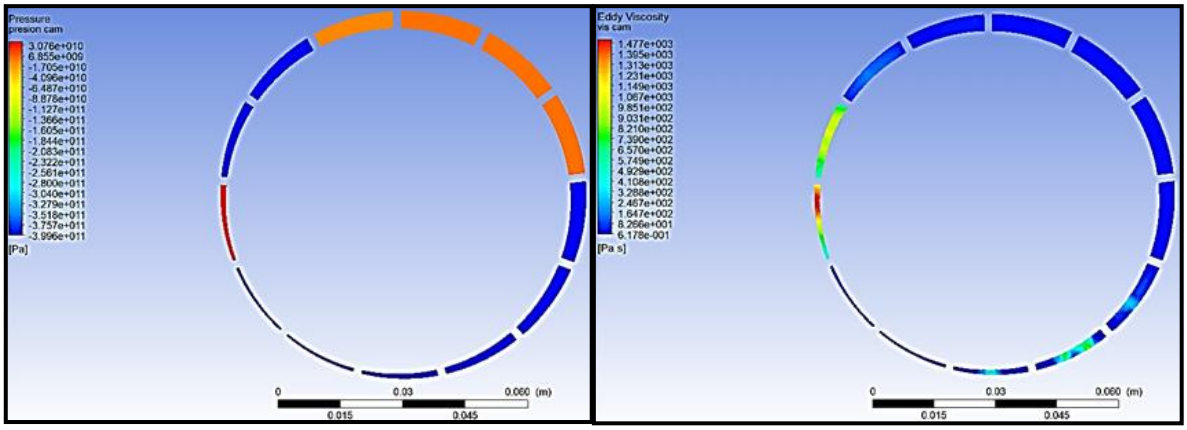

Figure 16. Left: Pressure profile for the internal chamber, first model, right: Turbulent viscosity profile, for the inner chamber, third model.

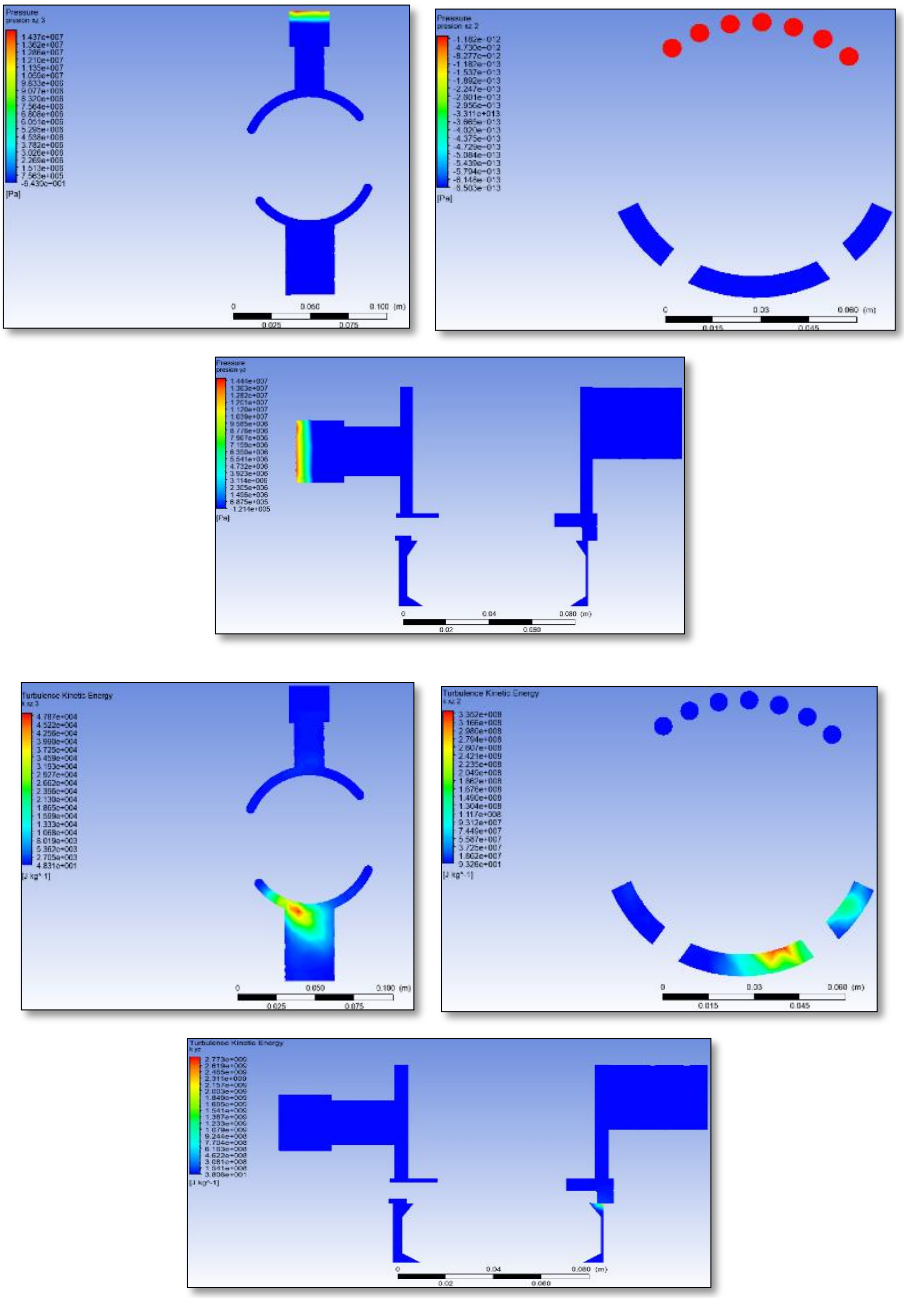

Figure 17. Pressure profiles, turbulent kinetic energy and dissipation of turbulent energy, in consecutive order respectively, sectional view of chamber, inlet and outlet, third model.

3.4. Fourth model, carried out with κ-ω

Just like the previous model, the results of the pressure at the pump outlet are taken directly, as shown in **Figure 18 (left)**. Considering the operating output pressure, under the same conditions, the pressure reaches a value of 140 bar. Therefore, the relative percentage error is:

$$E\% = \frac{|145\ bar - 140\ bar|}{140\ bar} * 100\% = 3.571\%$$

A relative percentage error of 3.571% was found, which demonstrates consistency within the validation of the pressure range for this model.

For the speed range, as shown in **Figure 18** (right), under the conditions proposed in this model, it can be seen that the results are

DOI: http://dx.doi.org/10.17509/ijost.v6i1.xxxx |
p- ISSN 2528-1410 e- ISSN 2527-8045 |

similar to the previous model, only that the profile is now more clearly defined and the distribution is better understood, as previously it was not very well defined towards the center of the output cavity. **Figure 19 (left)** shows that this model offers the best profile for pressure distribution in the chamber, compared to the four models carried out. The gradient linked to the clear definition of the suction and discharge side of the pump is evident in the figure. Also, notice the transition between each region when it approaches each critical area, which is aligned with what is intended with the physical phenomenon.

According to **Figure 19 (right)**, the definition of the turbulent viscosity is still not clear because only the suction area with high viscosity values is defined.

Finally, in **Figure 20**, the results for the same operating variables are shown for the sectioned view of the inlet, outlet, and internal chamber. According to the conditions proposed in this model and the previous model, the pressure profiles have a better definition because now, in the central image, there is a respective ejection gradient, and in the lateral images, the transition between high and low pressure is visible. Finally, in the turbulent kinetic energy, important details can be seen in the intake and suction lines; the effects of the geometry are clearly highlighted in this area.

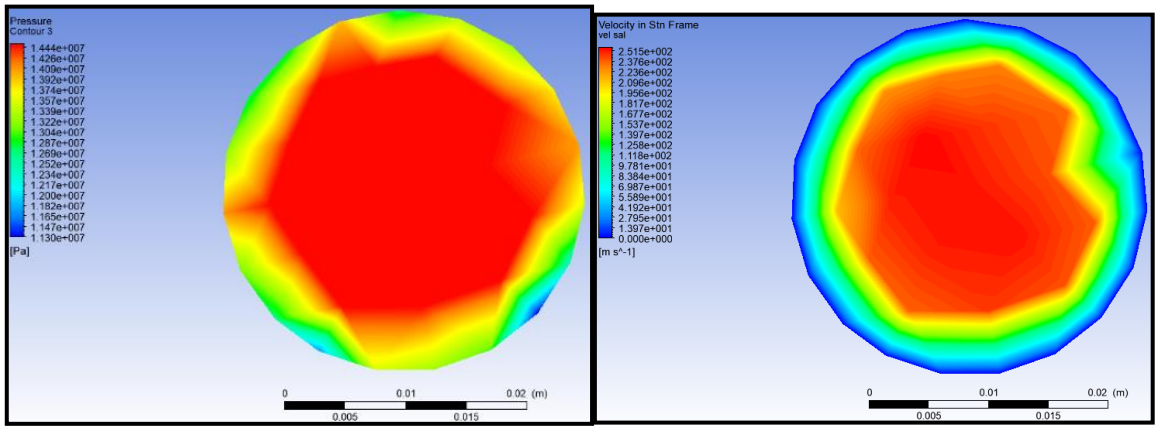

Figure 18. Fourth model – left: Outlet pressure profile, right: Speed profile at the output.

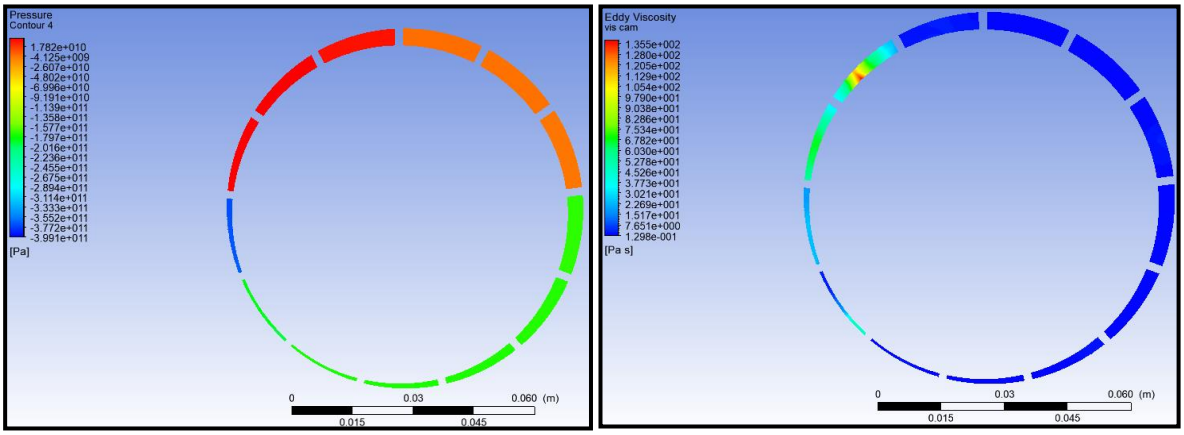

Figure 19. Left: Pressure profile for the internal chamber, first model, right: Turbulent viscosity profile, for the inner chamber, fourth model.

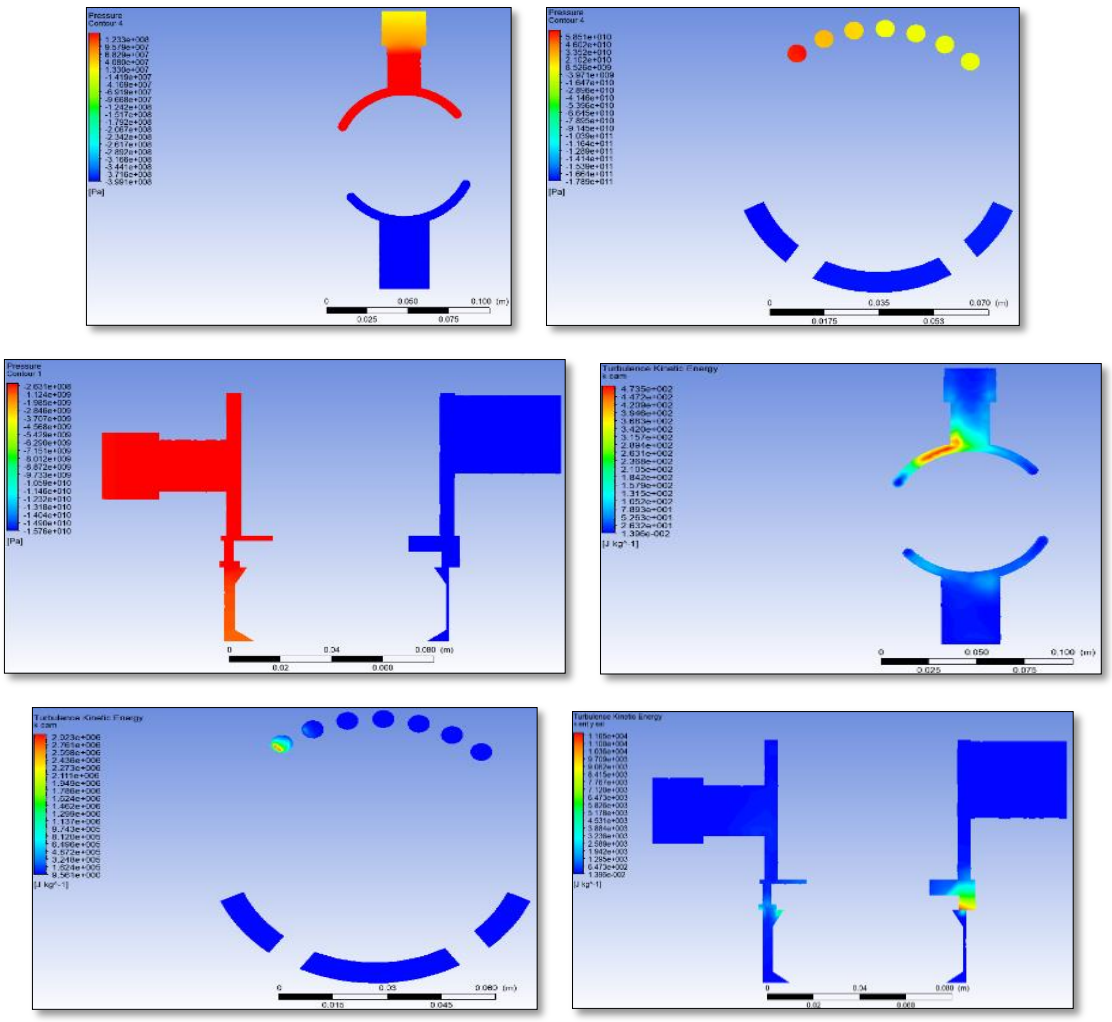

Figure 20. Pressure profiles, turbulent kinetic energy and dissipation of turbulent energy, in consecutive order respectively, sectional view of chamber, inlet and outlet, fourth model.

3.3. Fifth model, carried out with κ-ε

In a vane pump, its flow rate will not depend on the resistance in the pipe. The latter is a direct consequence of higher-pressure ranges which predominates in the system because, for a given fluid speed, the displacement will be the same, and therefore, the flow rate will also be the same; this is reflected in the characteristic curves of a vane pump, which clearly shows that the operating pressure should theoretically be kept constant, regardless of the flow variations. For the pump used in this study, the respective characteristic curve can be found on the official catalog and here it can be seen how the flow behavior is dependent on the operating pressure (output) at the pump.

Since an angular velocity value is set in this curve, the only possibility of flow variation is due to a change in eccentricity. The characteristic curve also shows a small pressure drop almost at the limit of the permissible flow. Since this is the real measurement, the pump material offers limitations in terms of mechanical resistance, and thus the pressure falls only when its

DOI: http://dx.doi.org/10.17509/ijost.v6i1.xxxx |
p- ISSN 2528-1410 e- ISSN 2527-8045 |

value is very high in relation to that allowed by the material.

With this in mind, the simulation is evaluated, and the results of the output pressure are shown in **Figure 21 (left)**, with an average output pressure of approximately $1.644009x10^7\ Pa$, or approximately 164 bar. Considering the operating output pressure, under the same conditions, it gives a value of 160 bar. Therefore, the relative percentage error is:

$$E\% = \frac{|164\ bar - 160\ bar|}{160\ bar} * 100\% = 2.5\%$$

A relative percentage error of 2.5% was found, which shows the consistency of the calculations. Therefore, the simulation is successfully validated under this result.

Continuing on to the speed, **Figure 21 (right)** shows concentrically distributed profiles at the exit, and in fact, suggests that the borders are where the greatest amount of viscosity exists, and therefore, the speed magnitude falls in this profile.

While a better result was obtained for the pressure, with respect to the previous models, the suction and discharge zone in the chamber is still not very clear because the vacuum zone must be present just after the part with the highest pressure due to the eccentricity at that point, although it is possible that the behavior is not so critical because the volume of the chamber was modified by the eccentricity. For the turbulent viscosity, the greatest magnitude of this value must be presented in the critical zone of the chamber. There are regions where the behavior of the viscosity is slightly defined as the system begins to rotate.

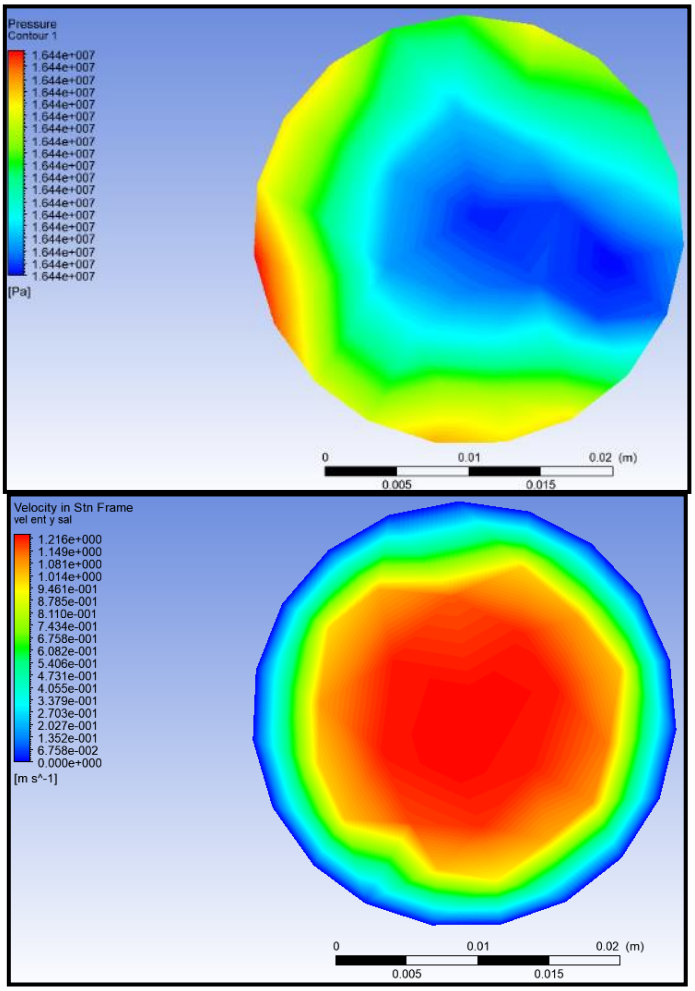

Figure 21. Fifth model – left: Outlet pressure profile, right: Speed profile at the output.

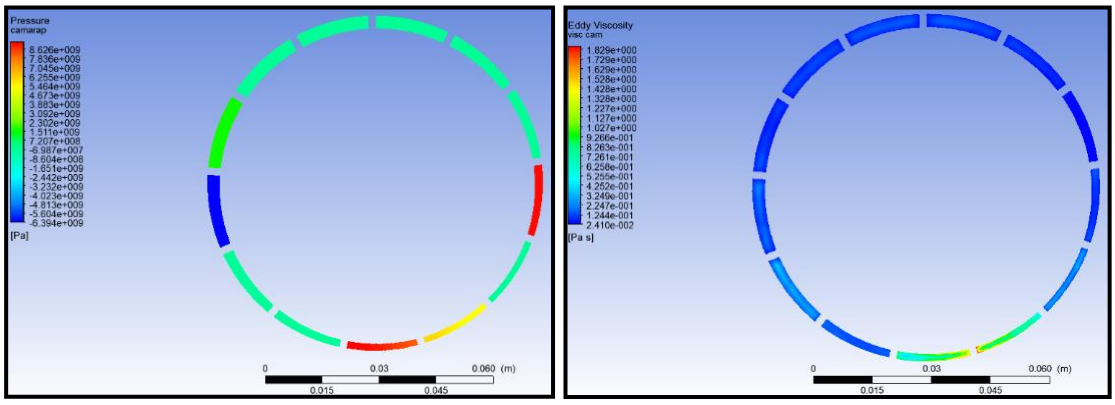

Figure 22. Left: Pressure profile for the internal chamber, fifth model, Right: Turbulent viscosity profile, for the inner chamber, fifth model.

Finally, **Figure 23** shows the results for the same operating variables for the sectional view of the inlet, outlet, and internal chamber. The pressure is normally seen as high and low with the expected value at the outlet, showing important effects related to the suction in the chamber as well. Border effects in the suction stage are clearly defined and can even be seen as the pressure gradient in the suction phase by the pump since the colored contour registers an excellent result that is evidenced from the suction area (blue, low pressure) to the inner part of the chamber (red, high pressure). Finally, the turbulent kinetic energy reveals important details regarding the suction cavity, due to its geometry, it demonstrates the importance of border effects; furthermore, in the three representations, there is a tendency for the results to define the same area, in this case, the suction side, since this is where the highest amount of viscosity is presented, as the fluid will tend to refuse to flow, under the influence of the pump.

3.4. Sixth model, carried out with κ-ω

For the sixth model, an average output pressure of approximately $1.5445081x10^7$ Pa was obtained **(Figure 24 at the left)**, which is about 154 bar. Considering the operating output pressure, which gives a value of 160 bar, the relative percentage error is:

$$E\% = \frac{|154\ bar - 160\ bar|}{160\ bar} * 100\% = 3{,}75\%$$

A relative percentage error of 3.75% was found, less than 5%. Therefore, the simulation is satisfactorily validated under these conditions.

For the speed at the outlet zone **(Figure 24 at the right)**, it is seen a clear disorder in the speed distribution but highlights a symmetrical condition of the profile. **Figure 25 (left)** shows a clearer definition of the pressure profile in the chamber than the previous model because the suction side is clearly defined in contrast to the discharge side. According to **Figure 25 (right)**, important results are obtained for the turbulent viscosity as on this occasion, in addition to defining the critical zone, other types of zones are also defined in the chamber, enhancing the preference of this model for the simulation. **Figure 26** shows that the pressure is normally seen as high and low with the expected value at the discharge, also showing important effects related to the suction in the chamber. The definition of aspects related to suction is preserved in the *speed*, and turbulent kinetic energy reveals the loss of energy present in the abrupt changes of geometry in the pump.

DOI: http://dx.doi.org/10.17509/ijost.v6i1.xxxx |
p- ISSN 2528-1410 e- ISSN 2527-8045 |

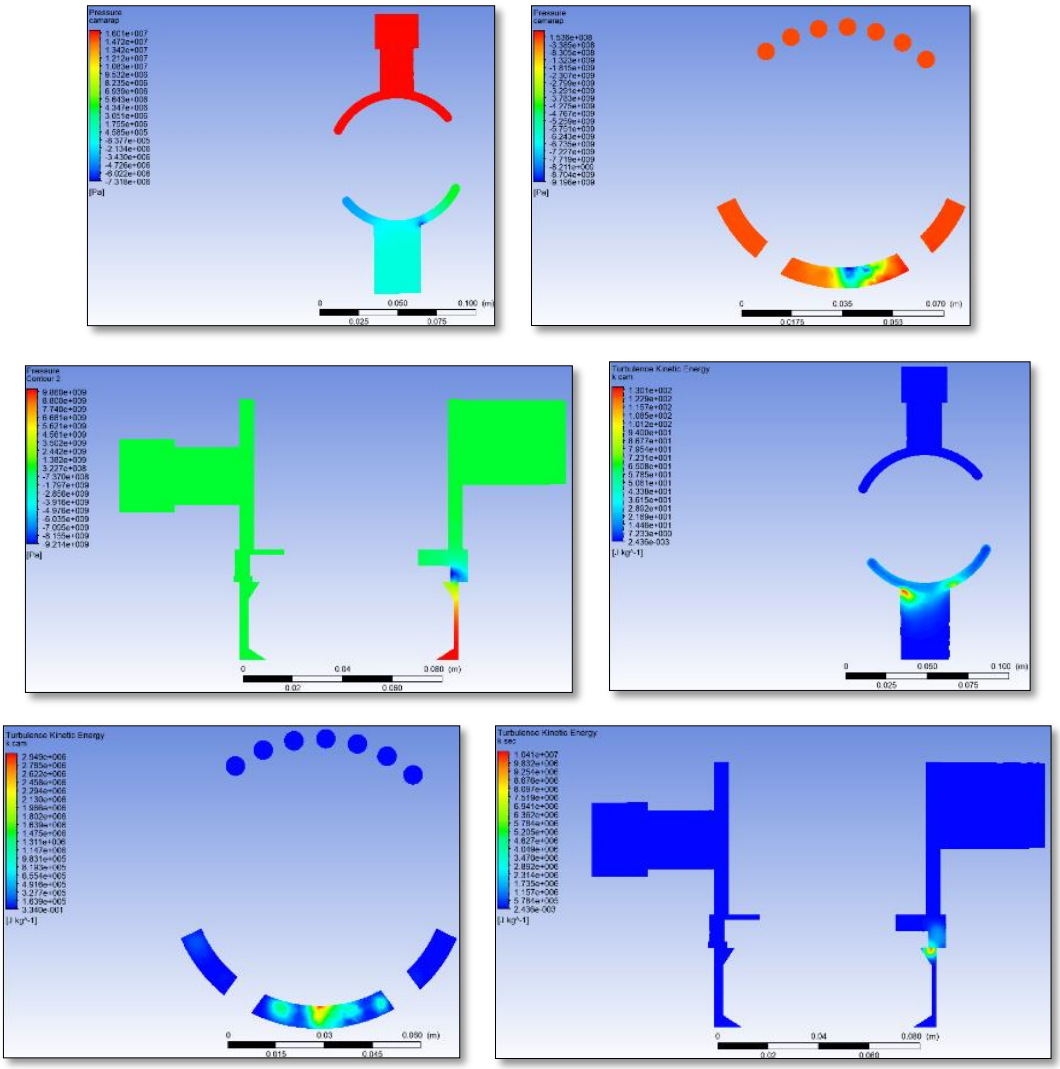

Figure 23. Pressure profiles, turbulent kinetic energy and dissipation of turbulent energy, in consecutive order respectively, sectional view of chamber, inlet and outlet, fifth model.

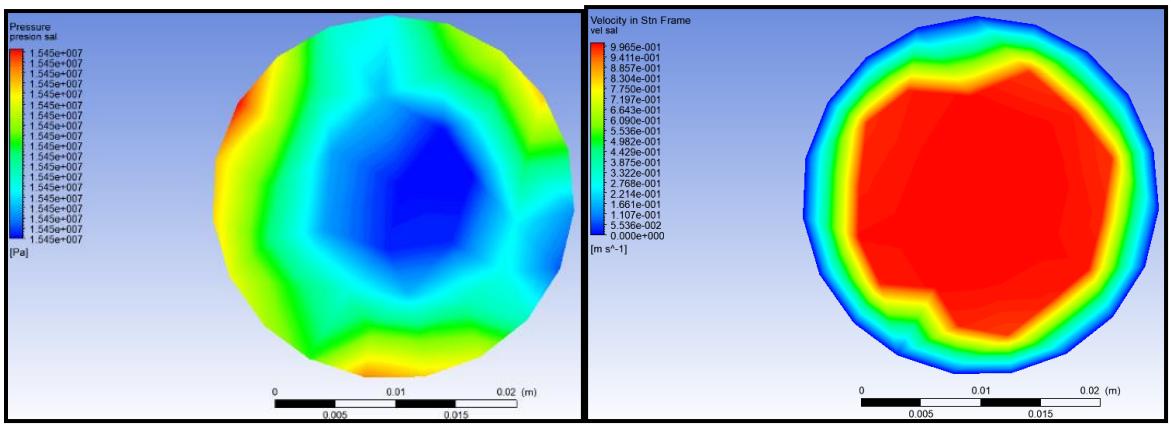

Figure 24. Sixth model – left: Outlet pressure profile, right: Speed profile at the output.

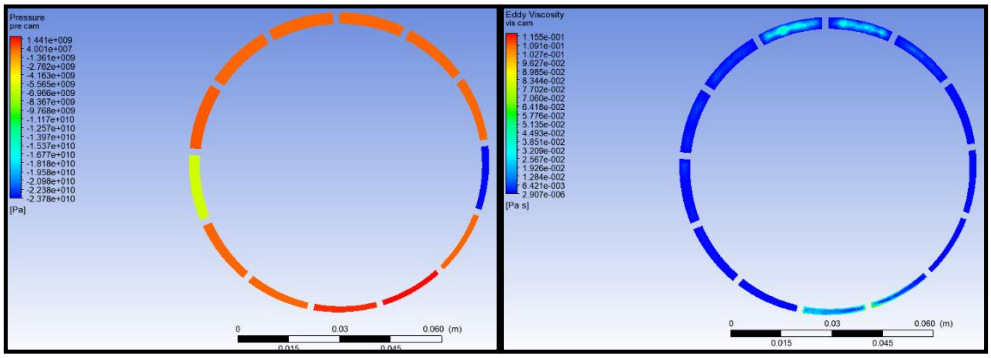

Figure 25. Left: Pressure profile for the internal chamber, first model, Right: Turbulent viscosity profile, for the inner chamber, Sixth model.

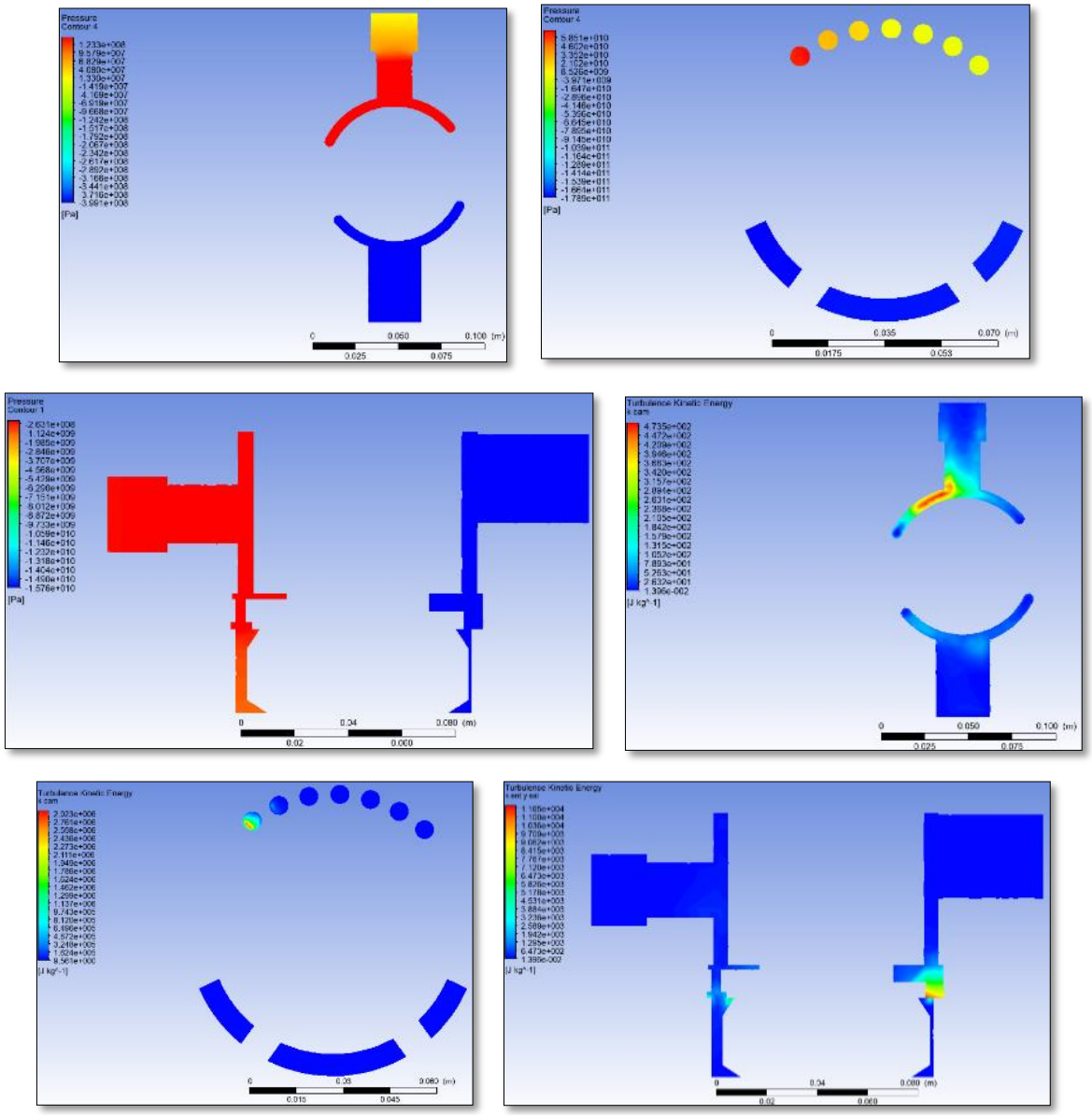

Figure 26. Pressure profiles, turbulent kinetic energy and dissipation of turbulent energy, in consecutive order respectively, sectional view of chamber, inlet and outlet, Sixth model.

DOI: http://dx.doi.org/10.17509/ijost.v6i1.xxxx |
p- ISSN 2528-1410 e- ISSN 2527-8045 |

4. CONCLUSION

The investigation focused on a CFD analysis using different turbulence models, namely using k-ε and k-ω to examine the hydraulic performance of a vane pump. Specifically, Solidworks® was used for the CAD design, while ANSYS® powered the computational domain, mesh generation, and CFD turbulence simulations. The comparative assessment of the turbulence models stands as a remarkable aspect from former research, while the incorporation of variable angular velocity and concentricity emerge as unique aspects of the investigation. The results demonstrated that both models can be validated accurately with a relative error of less than 5%.

Among the parameter analyzed, the density distribution was found to be constant along the computational domain, whereas the velocity profile was almost invariable. This behavior can be explained due to the functionality of the vane pump that governed the operational parameters based on geometrical features. Regarding turbulence model performance, the k-ω provides the best performance while describing the contour distributions of the parameters analyzed, which demonstrates that it accurately accounts for edge effects, energy losses in the walls, and turbulent viscosity. Contrarily, the conventional k-ε model showed enhanced performance while describing the pressure gradients in the chamber. The fashion mainly provides an appropriate prediction of the pressure gradients in the suction and discharge areas of the chamber. The simulations performed with a different angular velocity displayed strong variations in the velocity, viscosity, and turbulent energy profiles, which is a direct indication of higher predictability of the swirl formation. On the other hand, the simulations computed with a variation of the eccentricity revealed a decreasing trend in the vacuum pressure effect in the chamber.

In future studies, a more precise description of energy effects could be analyzed in the CFD modeling which can reveal important information about the thermal-hydraulic performance of vane pumps as an initial step for optimization.

5. ACKNOWLEDGMENT

The present investigation was supported by Universidad del Atlántico (Barranquilla, Colombia).

6. AUTHORS' NOTE

The author(s) declare(s) that there is no conflict of interest regarding the publication of this article. The authors confirmed that the data and the paper are free of plagiarism.

7. REFERENCES

Ahmed, A., and Demoulin, M. (2002). Turbulence modelling in the automotive industry. *Engineering Turbulence Modelling and Experiments*, *5*(2002), 29–42.

Chima, R. O. D. R. I. C. K. V. (1995). A k-omega turbulence model for quasi-three-dimensional turbomachinery flows. *34th Aerospace Sciences Meeting and Exhibit*, *248*(1995), 1-13.

Feng, J., Benra, F. K., and Dohmen, H. J. (2010). Application of different turbulence models in unsteady flow simulations of a radial diffuser pump. *Forschung Im Ingenieurwesen/Engineering Research*, *74*(3), 123–133.

Frosina, E., Senatore, A., Buono, D., Manganelli, M. U., and Olivetti, M. (2014). A tridimensional CFD analysis of the oil pump of an high performance motorbike engine.

Energy Procedia, *45*(2014), 938–948.

Lan, X. K., Khodadadi, J. M., and Shen, F. (1997). Evaluation of six κ-ε turbulence model predictions of flow in a continuous casting billet-mold water model using laser Doppler velocimetry measurements. *Metallurgical and Materials Transactions B: Process Metallurgy and Materials Processing Science*, *28*(2), 321–332.

Mangani, L., Casartelli, E., and Mauri, S. (2011). Assessment of various turbulence models in a high pressure ratio centrifugal compressor with an object oriented CFD code. *Proceedings of the ASME Turbo Expo*, *7*(Parts A, B, And C), 2219–2229.

DOI: http://dx.doi.org/10.17509/ijost.v6i1.xxxx |
p- ISSN 2528-1410 e- ISSN 2527-8045 |